Scientific Reports
https://doi.org/10.1038/s41598-026-63870-9

Article in Press

3D-printed meta-matching layer for enhanced ultrasound transmission through calcified plaques: a phantom study

Received: 23 January 2026

Accepted: 21 July 2026

Published online: 17 August 2026

Cite this article as: Ghanbarzadeh-Dagheyan A., Dong E., Ghanami M. *et al.* 3D-printed meta-matching layer for enhanced ultrasound transmission through calcified plaques: a phantom study. *Sci Rep* (2026). https://doi.org/10.1038/s41598-026-63870-9

Ashkan Ghanbarzadeh-Dagheyan, Erqian Dong, Maral Ghanami, Chen Shen & Nicholas X. Fang

3D-Printed Meta-Matching Layer for Enhanced Ultrasound Transmission Through Calcified Plaques: A Phantom Study

Ashkan Ghanbarzadeh-Dagheyan[1,2,+,*], Erqian Dong[3,+], Maral Ghanami[4], Chen Shen[4], and Nicholas X. Fang[3]

[1]Biomedical Photonics Imaging (BMPI), Multimodality Medical Imaging (M3i), and Physics of Fluid (PoF), University of Twente Enschede, the Netherlands
[2]TechMed Research Center, University of Twente Enschede, the Netherlands
[3]Department of Mechanical Engineering, University of Hong Kong Pok Fu Lam, Hong Kong
[4]Department of Mechanical Engineering, Rowan University, Glassboro, NJ, USA
[*]a.dagheyan@utwente.nl
[+]These authors contributed equally to this work

ABSTRACT

Calcified plaques strongly reflect ultrasound waves, limiting visualization of structures located behind them. This proof-of-concept work presents one of the first demonstrations of a directly 3D-printed meta-matching layer (MML) designed for medical ultrasound frequencies (4 MHz) to improve transmission through calcified plaque-like structures. The MML employs subwavelength microstructures to create a gradient acoustic impedance, reducing reflections and enhancing acoustic transmission. Numerical optimization and experimental validation demonstrated strong agreement. At 4 MHz, the optimized 10-μm-resolution MML increased relative transmission by approximately 192% and reduced relative reflection by approximately 77% compared with the aberrating layer alone. Ultrasound imaging confirmed improved signal penetration into the vessel lumen and preservation of downstream vessel visibility. Although image artifacts introduced by the structured interface currently limit robust flow quantification, this proof-of-concept study demonstrates the feasibility of patient-specific, add-on metamaterial layers for enhancing ultrasound transmission through highly reflective vascular structures.

Introduction

Acoustic metamaterials—artificially structured media engineered at sub-wavelength scales—have greatly expanded control over sound waves, enabling phenomena such as negative refraction, focusing beyond the diffraction limit, cloaking, and acoustic sensing[1–5]. Over the past two decades, acoustic metamaterials have made significant contributions to the fields of sound absorption and noise reduction[6], as well as underwater acoustic energy manipulation[7]. Additionally, acoustic metamaterials have gradually evolved into lightweight and compact metasurface structures, thereby laying a solid foundation for extending their applications to the medical ultrasound frequency range. In medical ultrasound, where operational frequencies typically range from 1 to 10 MHz, the subwavelength requirement translates to feature sizes of tens of micrometers—an order of magnitude smaller than most conventional airborne acoustic metamaterial applications. Thus, despite proof-of-concept demonstrations in other fields, translating metamaterials to MHz ultrasound remains challenging due to fabrication constraints at micrometer scale[8,9]. This fabrication bottleneck represents a critical gap in the deployment of ultrasound metamaterials for clinical imaging and therapy. For medical imaging, going through highly reflective or aberrating layers such as bone or calcified plaques is of hight interest.

There are many innovative solutions to enhance transmission and reduce reflection in ultrasound applications. For example, gradient acoustic-impedance matching layers are effective in minimizing reflections at material interfaces. Continuously varying impedance matching layers have been shown to reduce reflections through smooth acoustic transitions between dissimilar media[10]. A prime example is the cone-structured metamaterial layer developed for ultrasound probes, which creates a continuous impedance gradient across the layer by etching silica fibers into tapering cones[11]. This study demonstrated over 100% fractional bandwidth gain in a MHz-range transducer by bridging piezoelectric and tissue impedances. More recently, metamaterial-integrated bioadhesive hydrogel transducers have employed a gradient impedance transition between piezoelectric elements and tissue to improve acoustic transmission and bandwidth, further highlighting the potential of metamaterial-based impedance engineering in biomedical ultrasound[12]. Complementary approaches include phononic-crystal-based gradient layers for broadband matching[13], Helmholtz resonator architectures for phase-corrected beam shaping[14] and enhanced transmission[9], and acoustic holography[15], which have potential for the MHz regime as well. In addition, iterative angular spectrum-based holography has been introduced from Fourier optics into ultrasound holograms[16]. Bifocal acoustic holograms have demonstrated potential in bilateral blood-brain barrier opening as one typical example of aberration layers[17]. However, their fundamental limitation lies in the introduction of resonant metamaterials, where the emission response is maximized only at specific frequencies. This often makes it challenging to cover the bandwidth range of the impulse response of medical imaging probes.

As such, additive manufacturing of metamaterial matching layers remains an open area of exploration, with complementary acoustic metamaterials and gradient impedance matching layers applied to medical problems such as transcranial ultrasound focusing[18,19]. In one study, a multi-layer metamaterial was 3D-printed to correct skull-induced aberrations[18], while another used a 3D-printed mold to fabricate a powder-based gradient matching layer to improve transmission through the skull[19]. These studies are constrained by the precision limits of traditional 3D printing techniques operating in the MHz frequency range. Achieving sub-100 µm resolution to accommodate MHz-range ultrasonic devices imposes fundamental limitations on the design of meta-matching layers using conventional 3D printing technologies.

Among different applications that could benefit from transmission-enhancing metamaterials, vascular imaging is a particularly interesting case. In vascular ultrasound imaging, calcified plaques introduce strong acoustic impedance mismatches causing reflection and attenuation, creating dark acoustic shadows in downstream regions[20,21]. Shadow artifacts impede accurate blood-flow quantification using ultrasound velocimetry[22]. Active compensation methods like ISAAC ("Iterative Scheme for Active Attenuation Correction") by Plomp *et al.* iteratively boost transmitted power locally, successfully recovering signal strength in echo-PIV datasets[23]. However, these techniques tend to increase reflection from highly calcified tissues, limiting their efficacy when plaques are strongly reflective[24]. Passive, gradient, subwavelength-microstructured meta-matching layers (MMLs), by contrast, may offer potential to enhance forward transmission without amplifying back-reflections.

From a theoretical perspective, such graded matching layers can be described using the framework of wave propagation in media with continuously varying acoustic impedance. In this approach, the structure is treated as an equivalent transmission line with a spatially dependent impedance $Z(x)$ along the propagation direction $x \in [0, L]$, where L is the thickness of the matching layer. For sufficiently smooth impedance variations (i.e., in the slowly varying or WKB approximation), the reflection coefficient can be approximated as[25,26]

$$R \approx \frac{1}{2} \int_0^L \frac{1}{Z(x)} \frac{dZ(x)}{dx} e^{-2j\beta x} \, dx, \tag{1}$$

where $\beta = \omega/c$ is the wavenumber in the medium, ω is the angular frequency, c is the wave speed, and j is the imaginary unit. This expression shows that reflections are governed by the spatial rate of change of impedance, dZ/dx, such that smoother transitions reduce back-reflections compared to abrupt interfaces. This principle forms the basis of tapered transmission line theory and optimal matching profiles such as the Klopfenstein taper and the matching layer in the present study. Conventional implementations of such graded matching typically rely on material layering or fabrication-specific designs with limited tunability[27,28]; in contrast, the present work aims to employ a subwavelength microstructured approach in which the effective impedance profile is governed by geometry, enabling continuous gradients and systematic design within a single printable material.

In Fig. 1-(a) an in-vitro model of an artery (printed in Flexible 80-A, Formlabs, USA) and a highly reflective plaque (printed in Clear V4, Formlabs, USA) is shown. As observed in Fig. 1-(b), in the plaque-free model, the image of contrast agents (microbubbles) is clear and can be processed into a vector field after high-frame-rate ultrasound acquisition. However, a dark shadow is present in the image of the model with the plaque, as Fig. 1-(c) depicts, impeding correct ultrasound velocimetry, leading to an erroneous velocity field and an upward displacement.

This work introduces an add-on, directly 3D-printed meta-matching layer (MML) with a gradient impedance engineered to improve ultrasound transmission through calcified plaques. The triangular structures in gradient matching layers act as a structured impedance-transition interface that improves acoustic transmission through highly reflective layers. The use of triangular unit cells results in an approximately linear variation of the effective impedance, corresponding to a constant impedance gradient dZ/dx. Such linear tapers are widely used as practical approximations of continuously graded matching layers, offering a balance between broadband reflection reduction and fabrication simplicity. The term "meta" is used here as the features of the designed matching layer are sub-wavelength and the optimization process is performed on a unit-cell basis. In Fig. 1-(d), a schematic of a carotid artery is displayed, with a calcified plaque highlighted in Fig. 1-(e). This motivates the central research question: can a structured, patient-specific MML improve acoustic transmission through highly reflective plaques?

With this long-term objective in mind, the present work reports a preliminary *in-vitro* investigation of this concept using

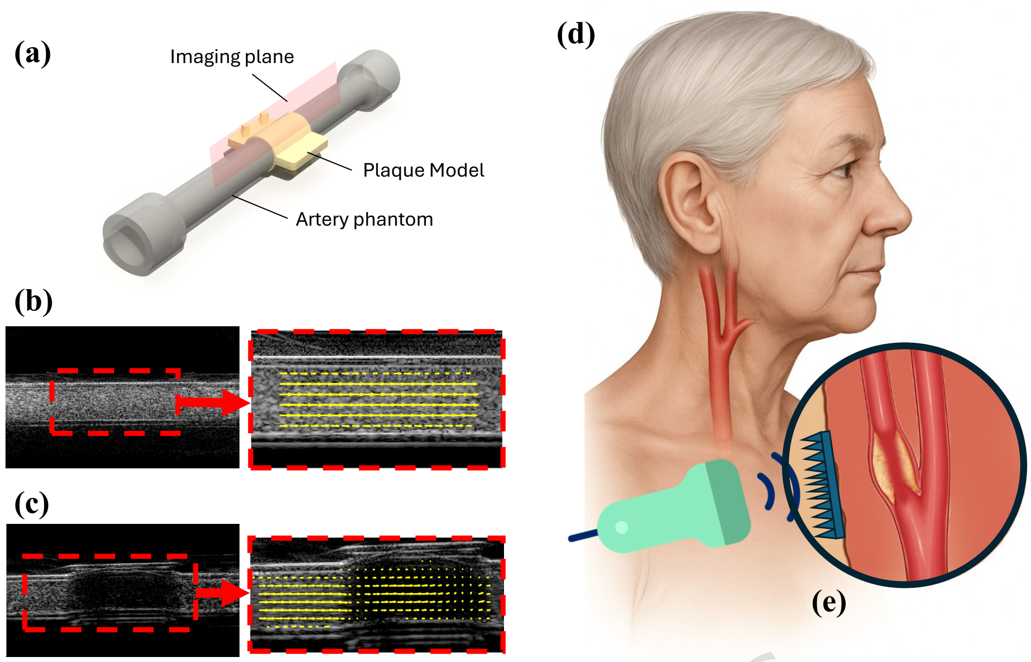

Figure 1. Shadow behind calcified plaques and a potential solution as the motivation behind this research: (a) Model of an artery (6 mm in diameter) and a reflective, attenuating plaque around it. Ultrasound image of microbubbles in (b) the plaque-free artery model and a velocity field as the output of echoPIV and (c) the artery model with the plaque and its associated velocity field. (d) Schematic of a calcified plaque in the carotid artery and (e) a customized meta-matching layer to image through the plaque. [*Schematic illustration in (d) and (e) created by the authors using AI-generated artwork and icons from flaticon.com*]

arterial phantoms and iterative, simulation-driven designs. The proposed approach is first evaluated numerically to establish the underlying transmission-enhancement mechanism, followed by experimental validation using additively manufactured samples. To isolate and investigate the fundamental transmission-enhancement mechanism of the proposed MML, the design was performed using a simple aberration layer (SAL) representing a highly reflective calcification-like structure. At first, an MML is designed and fabricated based on simplified assumptions, such as having no loss and acoustic-solid interactions. Discrepancies between simulated and measured performance are then analyzed to identify key contributing factors, including material attenuation and fabrication-induced geometric variations. Using these analyses, an optimized MML is designed, fabricated, and examined.

The remainder of the paper is organized as follows: the Results section presents the simulation and experimental outcomes of the MML, followed by a Discussion of the governing mechanisms, limitations, and practical considerations, while the Methods section provides details of the numerical and experimental procedures.

Results

This section systematically evaluates the proposed meta-matching layer (MML) to establish the underlying transmission-enhancement mechanism. The details of the design methodology, fabrication, and experimental procedures are provided in the Methods section. We begin by analyzing an initial, iterative MML design using numerical simulations to assess its ability to improve acoustic transmission and reduce reflection at a highly mismatched interface. This is followed by experimental validation using additively manufactured samples, enabling direct comparison between simulated and measured acoustic performance. Observed discrepancies between the numerical and experimental results are then investigated to identify key contributing factors, including material attenuation and fabrication-induced geometric variations. Based on these findings, a refined, optimized MML design is developed and evaluated to improve agreement between simulation and experiment. Together, these steps provide a comprehensive assessment of the proposed approach, from initial concept to experimentally validated and refined design, and to assess the MML potential for improving imaging through highly reflective structures.

First MML Performance

Figure 2-(a) shows an schematic geometry of the designed MML (details in Methods), and Fig. 2-(b) shows its wide-band performance, exhibiting near-one transmission and near-zero reflection coefficients, under ideal conditions. Figure 2-(c) shows improved transmission through the plaque model into the artery lumen at 3 MHz, while Fig. 2-(d) confirms how the reflections off the MML are subdued in time domain when compared to a simple aberration layer (SAL) of the same material.

The first effort to fabricate this MML, 3D-printed on top of a 1-mm SAL of the same material, is shown in Fig. 2-(e). Note the layered structures of the MML as part of the printing process. The attenuation (dB) of ultrasound waves through the fabricated MML on top of the 1-mm SAL, measured in a two-transducer, water-tank setup, is plotted in Fig. 2-(f). This attenuation takes into account the effect of both reflection off and loss through the material. Two fabrication trials of the MML (MML #1 and #2) are compared with two fabrication trials of SALs (SAL #1 and #2). It is clear that unlike the numerical predictions, the attenuation through the MML-equipped SAL has increased, which requires scrutinization.

Ultrasound images of flowing microbubbles within the lumen of the artery phantom, averaged over 50 frames, are shown in Fig. 2-(g) for both the SAL (top row) and MML #1 (bottom row). These images, upon first impression, reveal that the shadow is increased when the MML is added to the SAL, as predicted by Fig. 2-(f). However, clearly, the reflection off the MML is less than the SAL across all frequency. To quantify the effects, using an image-based approach, the ratio of the average image intensity in the shadow (orange), non-shadow (yellow), and reflection (red) regions were calculated and the shadow and reflection averages were divided (normalized) by the non-shadow average, as reference. In the case of no aberration layer or MML (plaque-free) model, the same regions were considered to calculate the averages. Note that image intensity is directly proportional to signal intensity. Figure 2-(h) and -(i) respectively show the shadow and reflection ratios. Indeed, the image intensity under the plaque has decreased in the case of the MML, when compared to the plaque-free or SAL models. Conversely, the MML outperforms the SAL when it comes to reflection.

To troubleshoot the significant difference between the numerical and experimental results, a series of experiments were carried out to pinpoint the cause. These experiments and their ensuing results are presented in **Supplementary Materials A**, showing clearly that loss is the main reason behind the numerical-experimental gap. This finding informed steps for the second design, as described in the following subsection.

Optimized MML Performance

Figure 3 shows the optimization process of the MML, taking into account the effect of loss and acoustic-solid interactions (ASIs). Figure 3-(a) shows the geometry to be optimized for values of the triangular unit cell height (h) and width (w) and the lines over which transmission and reflection coefficients were calculated. The results of the optimization for 260 combinations of h and w values, normalized by the wavelength at 4 MHz (target imaging frequency) are shown in Fig. 3-(b), -(c), and (d). Going from Fig. 3-(b) to (d) the complexity of the numerical model increases: in (b), there is no loss and ASIs; in (c), only loss in considered, and in (d) both loss and ASIs are modeled. Based on this modeling, the optimal values from the most comprehensive model are $h^* = 0.3\lambda_{4MHz}$ and $w^* = 0.5\lambda_{4MHz}$, with λ_{4MHz} being the wavelength at 4 MHz in the MML. These correspond to optimal numeric values of $h = 191.25\ \mu m$ and $w = 318.75\ \mu m$.

It should be noted that to determine this working frequency, a series of experiments revealed that with the L12-3v transducer (Verasonics, Kirkland, USA), the lowest frequency that would allow an accurate retrival of the velocity field was 4 MHz. Below this frequency (e.g., at 3 MHz) the velocity was largely underestimated even after SVD filtering (**Supplementary Materials B**).

With these values, the optimized MML, on top of a 1-mm SAL, was fabricated, with a precision of 10 μm (shown in Fig. 3-(e)). Samples with a resolution of 5 μm were also printed. Note the cleaner, non-layered print, due to lower values of the unit cell height and improved print settings. Figure 3-(f) depicts the attenuation plots of the MML-SAL models (one with 5 micron precision and three replicates with 10 μm precision) versus the SALs. One of the first things that catches the attention is how much the overall attenuation of the MML-equipped models have improved when compared to the non-optimal MML models in Fig. 2-(f). The other, and more important, observation is the bands (yellow and purple) in which the attenuation of the MML-equipped SALs is less than the SALs.

The imaging performance of the optimized MMLs are shown in Fig. 4. The images clearly show that the image intensity is stronger underneath the MML-equipped models when compared to the SAL models. No signficant difference can be detected between the two fabrication precisions of the MMLs (5 and 10 microns). The insets show how the unit cells of the MML are visible in the optimized models at certain frequencies. Quantitative results (Fig. 4-(b) and -(c)), similar to those in Fig. 3, reveal that normalized image intensity is stronger in the “shadow” regions when using the MMLs, and normalized reflection intensity is weaker than the SAL. At the design frequency of 4 MHz, the optimized 10 μm MML increased the relative transmission by approximately 192% and reduced the relative reflection by approximately 77% compared with the aberrating layer alone. Similarly, the 5 μm MML increased the relative transmission by approximately 150% and reduced the relative reflection by approximately 73%. These results quantitatively demonstrate the ability of the proposed MML to improve acoustic energy transmission through highly reflective structures.

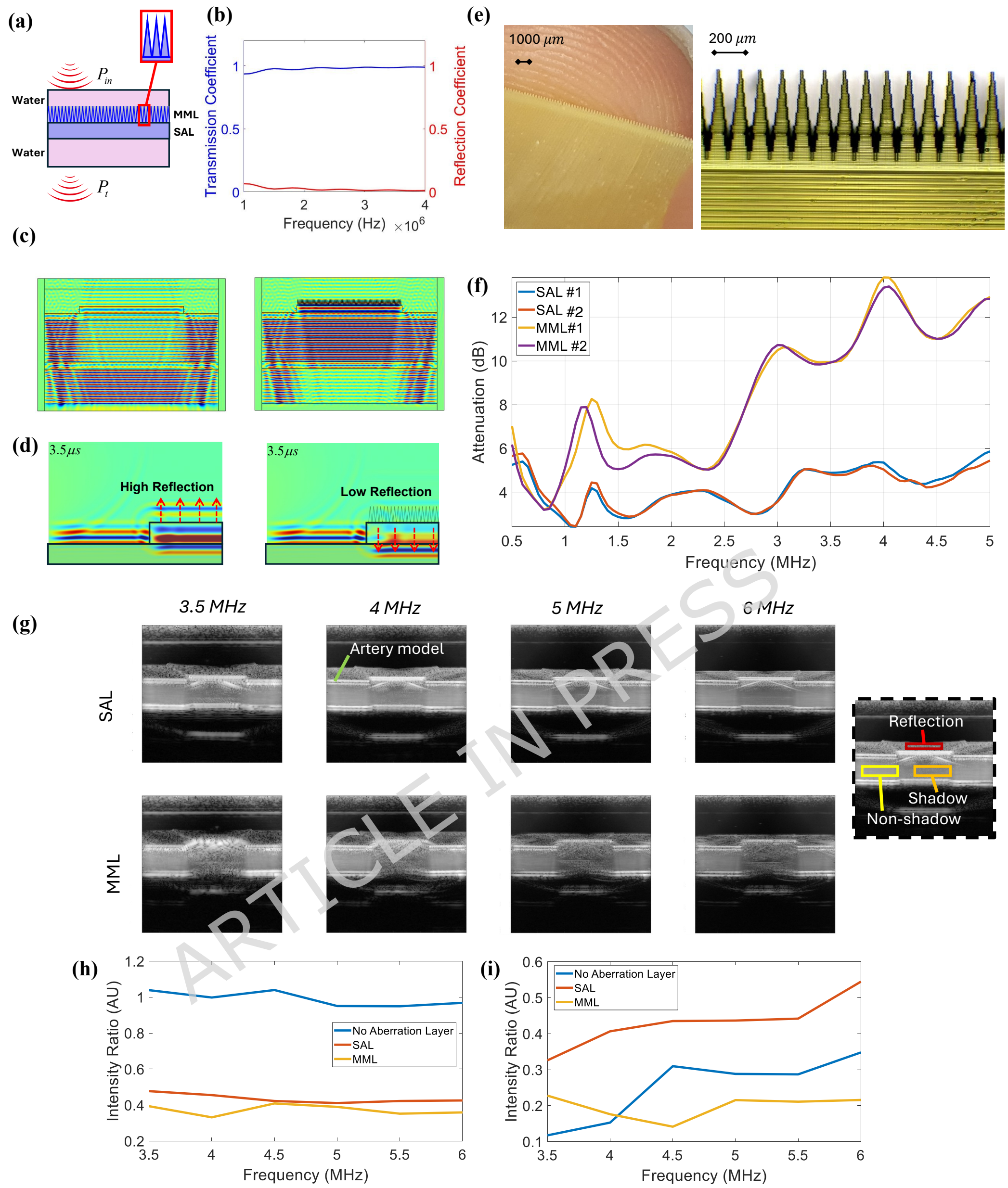

Figure 2. The first MML numerical and experimental performance: (a) The numerical geometry for the MML design, from top to bottom, assuming perfectly smooth surfaces: a layer of water, the MML, a 1-mm simple aberration layer (SAL), and a layer of water. (b) The broadband performance of the MML, assuming no attenuation. (c) The frequency domain simulation of the SAL (left) and the MML (right), showing transmission loss through the SAL and improved transmission through the MML. (d) The time domain simulation showing high reflection off the SAL and low reflection off the MML. (e) The first fabricated MML, showing the features of the print against a human finger (left) and the microstructures (right). (f) Experimental attenuation measurement of two SAL (#1 and #2) and two MML samples (#1 and #2). (g) Ultrasound imaging performance of the SAL (top row) versus the MML (bottom row), with regions (inset) of non-shadow, shadow, and reflection for quantitative analysis. (h) The ratio of image intensity in the shadow region to the non-shadow region. (i) The ratio of image intensity in the reflection region to the non-shadow region.

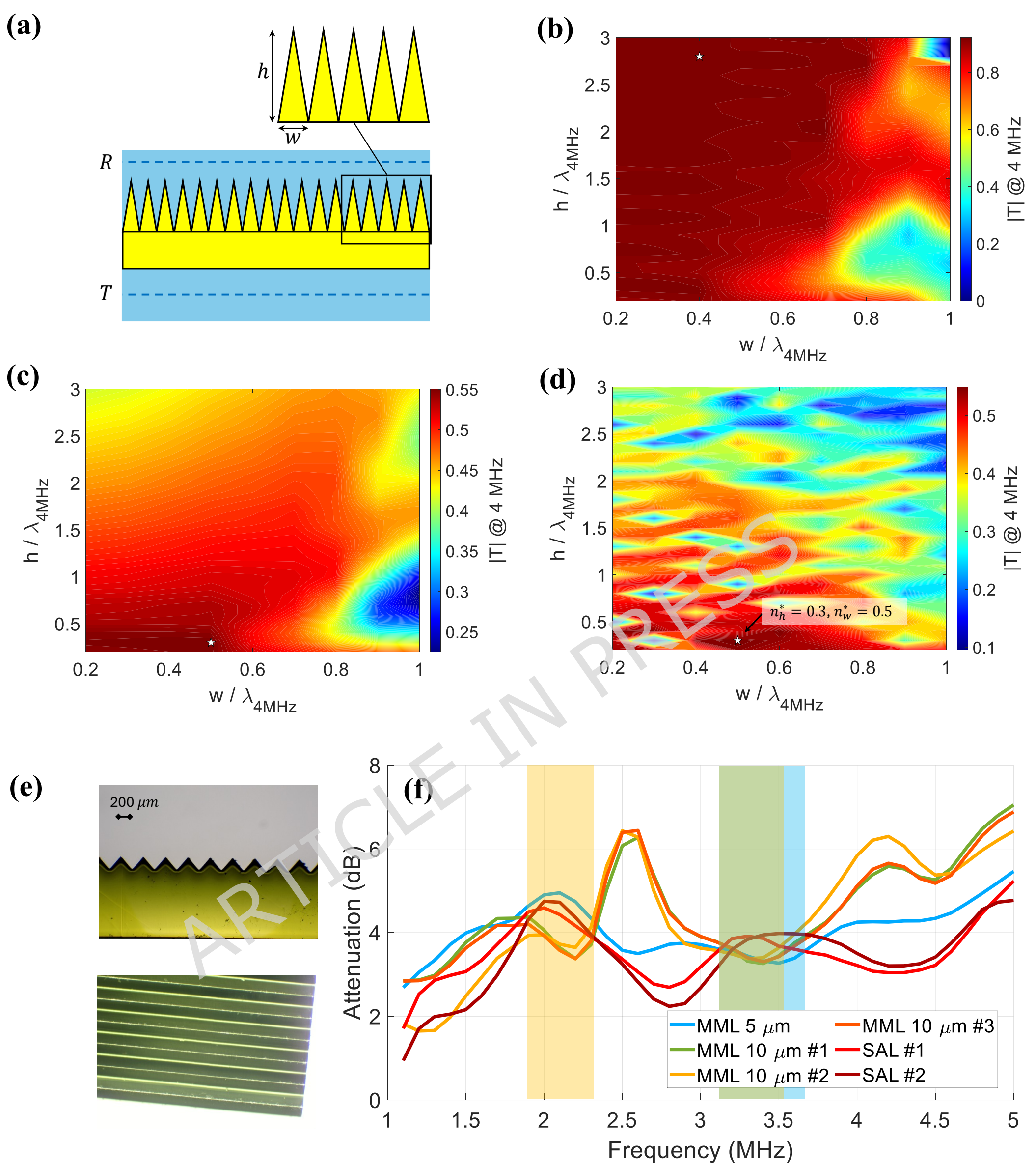

Figure 3. MML Numerical Optimization: (a) The optimization settings on the height (h) and width (w) of triangular unit cells of the MML. A model of the geometry is shown, where the MML is placed on top of a 1-mm aberration layer and the dashed lines T and R show where the transmission and reflection coefficients were measured. Subfigures show the transmission coefficient at 4 MHz (heat map) for various unit cell width (x axis) and height (y axis) for models with (b) no loss, (c) with loss, and (d) with loss and acoustic-solid interaction. (e) Fabricated optimal MML from side and top view. (f) Attenuation through various MML samples versus SAL samples, highlighting the bands where attenuation is notably improved by the MMLs.

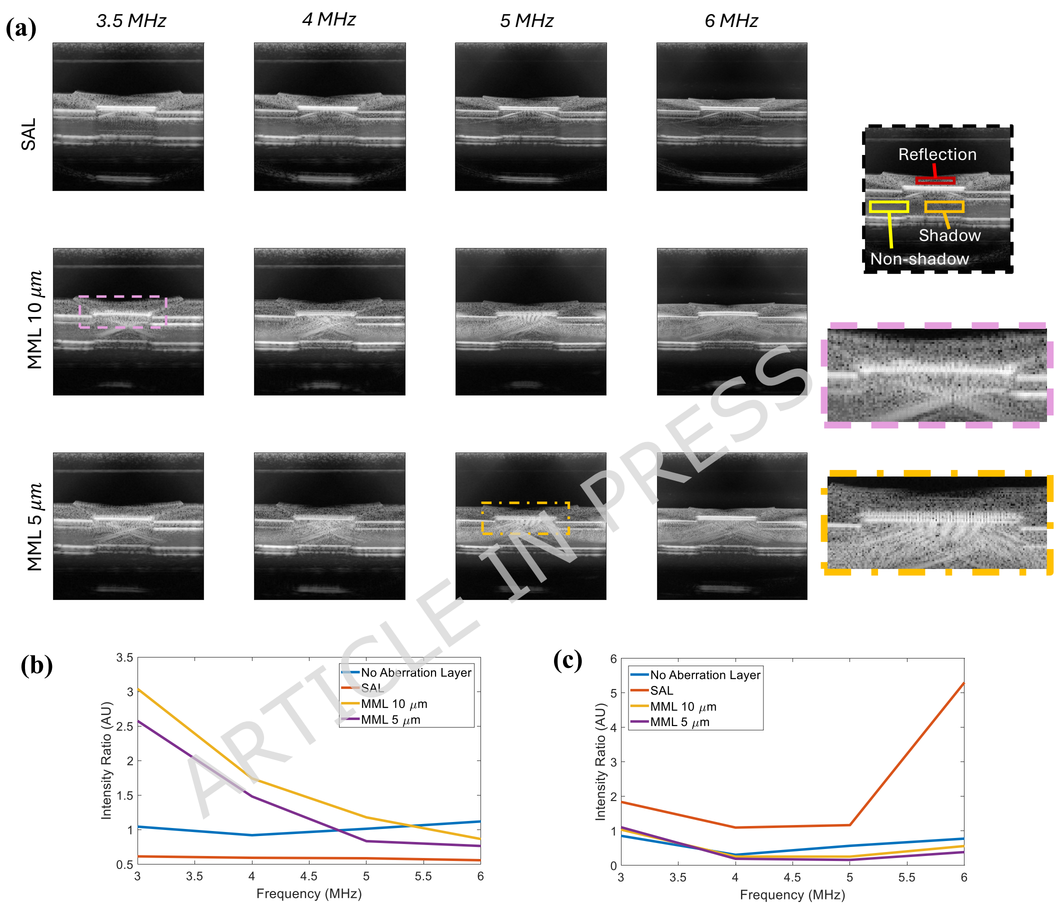

Figure 4. Optimized MML imaging performance: (a) Ultrasound images of the SAL (top row) versus the MML-10 micron (middle row) and the MML-5 micron (bottom row), with regions (inset, top) of non-shadow, shadow, and reflection for quantitative analysis. The insets (middle and bottom) show how the unit cells of the optimized MMLs are visible in the ultrasound image. (b) The ratio of image intensity in the shadow region to the non-shadow region. (c) The ratio of image intensity in the reflection region to the non-shadow region.

Discussions

This study reports the results of a 3D-printed meta matching layer (MML) for the purpose of improving transmission through and reflections off simplified models of arterial plaque models. The Discussions focus on understanding the discrepancy between the initial idealized simulations and experimental observations, highlighting the critical role of material loss and acoustic–solid interactions in shaping performance. We then relate these findings to the optimized design and its improved transmission and reflection behavior, while also addressing practical considerations such as fabrication-induced scattering, imaging artifacts, and model simplifications. Finally, the potential of this approach as a customizable, add-on solution for ultrasound imaging through highly reflective structures is discussed alongside its current limitations and directions for future work.

Numerical versus Experimental Results

The first trial of designing and fabricating such MMLs, as shown in Fig. 2, revealed a large gap between numerical predictions and experimental results. The numerical design assumed idealized triangular structures with smooth sidewalls and nominal dimensions of 550 µm in height and 150 µm in base width. Due to fabrication limitations of the additive manufacturing process, the printed structures exhibit visible layer steps and slight deviations from the designed geometry. The measured fabrication error in the final version of the first MML was approximately +10% in height and –5% in base width. In addition, the non-smooth sidewalls of the printed triangular features are expected to introduce additional acoustic scattering, which is also observable in the experimental measurements (Fig. 2(g)).

We also explored additional causes to explain difference between the performance of the simulated and 3D-printed MML. The list of potential causes included: MML in-plane and out-of-plane orientation with respect to the waves, water penetration into the unit cells, variation due to fabrication repeatability, and attenuation through loss, as discussed in **Supplementary Materials A**. Among these possible causes, it turned out that the main reason was neglecting loss in the simulations, as also confirmed by hydrophone-needle water tank measurements in **Supplementary Materials C**.

Many designs of acoustic metamaterials neglect intrinsic loss or acoustic-solid interactions to simplify the design process; however, several studies indicate that including loss can strongly affect both the predicted transmission and the attenuation bandwidth. For example, viscoelastic loss in locally resonant units alters band-gap positions and attenuation efficiency, so modelling material damping with appropriate constitutive models yields numerically more representative results[29]. Likewise, metamaterial designs targeting lossy biological barriers (e.g., skull or bone) require complex (real and imaginary) effective parameters or active compensation strategies to accurately predict transmission and reflection[30]. Including loss and acoustic-solid coupling in our second design iteration therefore brings the numerical model closer to experiments, consistent with prior work on lossy metamaterials.

Consequentially, in the second effort for the numeral design, more realistic settings were implemented: loss and acoustic-solid interactions. When compared to the model without loss (Fig. 2-(b)), it can be seen that the numerical values are more representative of the experimental results. In Fig. 2-(b), transmission coefficient ($|T|$) at 4 MHz is predicted to be 1, whereas the experimental results present a value of $|T| \approx 0.25$ (corresponding to an attenuation of ≈ 12 dB per thickness of MML #1). Yet, in the improved model, in Fig. 3-(d), $|T| \approx 0.55$ at 4 MHz, matching very well with $|T| \approx 0.56$ (corresponding to an attenuation of ≈ 5 dB for MML #1, optimal) in Fig. 3-(f). Comparing the results between Models (c) (loss only) and (d) (loss and ASI), it is clear that the introduction of ASI causes higher variations from one set of $h - w$ to another. Yet, interestingly enough, the optimal case in both models correspond to $w^* = 0.5\lambda_{4\ MHz}$ and $h^* = 0.3\lambda_{4\ MHz}$. The fabrication error in w and h was –5% and –14%, respectively, and there was no layered pattern (Fig. 3-(e)), which was present in the first MML (Fig. 2-(e)). While the improvement in the optimal MML-equipped SAL was not enough to surpass the attenuation value of the SAL at 4 MHz, Fig. 3-(f) shows that in the bands 1.9-2.3 MHz and 3.1-3.5 MHz, the MML-equipped SAL, despite the added thickness, outperforms the SAL.

Minor variations in attenuation observed among samples with the same nominal print resolution (Fig. 3(f)) are likely due to minor differences in sample alignment during measurements and fabrication-related inconsistencies, including small deviations in unit-cell geometry, surface roughness, and resin curing, which can affect effective acoustic properties and scattering. Interestingly, in the 1.8–2.3 MHz frequency band, the finer-resolution MML exhibits higher attenuation than the coarser counterpart. This behavior is mainly attributed to differences in the realized microstructure rather than resolution alone. The finer print more accurately reproduces sharp features and narrow gaps, which can enhance viscous and scattering-related losses, whereas the coarser print may effectively smooth or partially fill these features, resulting in lower effective attenuation in this band. In addition, small variations in curing conditions, resin distribution, and potential partial filling or trapping within microstructures may further increase local dissipation and contribute to the observed difference.” Overall, the optimized MML achieves a transmission coefficient of $|T| \approx 0.56$ at 4 MHz, in close agreement with loss-informed simulations, and exhibits lower attenuation than the baseline SAL in the 1.9–2.3 MHz and 3.1–3.5 MHz frequency bands, despite the added structural thickness.

The ultrasound imaging results of the optimized MML were also promising. Referring to Fig. 3-(g) to (i) for the non-optimized MML, one can observe that the non-optimized MML-equipped SAL does not outperform the SAL in terms of transmission, in agreement with the high attenuation values in Fig. 3-(f). However, the reflection off the MML is lower than the SAL. This is likely due to increased scattering caused by the small features (unit cells) of the MML that dissipate the energy in various angles rather than the perpendicular direction back to the ultrasound transducer. Thus, beyond conventional impedance matching, the microstructured geometry of the MML introduces additional wave phenomena that contribute to its performance. While the gradual impedance variation reduces reflections by minimizing abrupt interfaces, the subwavelength unit-cell features are also expected to redistribute a portion of the reflected energy into non-specular directions. This reduces coherent back-reflection toward the transducer, effectively lowering the measured reflection intensity. At the same time, this redistribution is accompanied by increased scattering within the structure, which can contribute to the observed image artifacts.

The optimized MML maintains this low-reflection advantage while increasing the transmission through the SAL, as shown in Fig. 4-(a) to (c). This is clear not only by looking at the quantitative results, but also noticing the high intensity of the image in the shadow region and the fact that the lower wall of the artery is visible underneath the optimized MMLs, whereas it is faded underneath the non-optimized MML (Fig. 3-(g)).

Practical Considerations and Limitations

Clinical Relevance. Clinical vascular ultrasound is commonly performed using linear-array transducers operating in the approximate range of 4–12 MHz, where increasing frequency improves spatial resolution but reduces penetration depth [21,31–33]. In the present study, 4 MHz was selected as the lowest frequency that still enabled reliable imaging of contrast agents and maximized penetration through highly reflective structures. This frequency is also consistent with previous clinical vascular flow-imaging studies employing contrast-enhanced ultrasound particle image velocimetry[21]. Although a direct comparison with commercial vascular imaging systems or probes is beyond the scope of this proof-of-concept study, the optimized MML increased relative transmission by approximately 192% and reduced relative reflection by approximately 77% compared with the aberrating layer alone, using the same probe (L12-3v). These improvements directly target acoustic shadowing caused by calcified plaques, a recognized limitation of conventional vascular ultrasound imaging. Furthermore, the measured attenuation of the tissue-mimicking aberration layer (2–6 dB over a thickness of 1–2 mm) falls within the range reported for calcified vascular tissues[34–36]. Consequently, the phantom provides a clinically relevant test environment for evaluating transmission-enhancement strategies in the presence of strong acoustic attenuation and reflection.

Clinical Translation and Patient-Specific Design. The principal contribution of this work is the proposed design framework that can be used to design MMLs for various cases. Because the optimal structural parameters depend on the acoustic properties and morphology of the targeted structure, future implementations will likely require application-specific or patient-specific designs. In clinical practice, heavily calcified plaques are routinely characterized using imaging modalities such as computed tomography angiography (CTA), which provide detailed anatomical information regarding plaque location, geometry, and extent, and ultrasonography, which provides attenuation and acoustic information. In principle, such information could be incorporated into the numerical optimization framework presented here to automatically generate customized MML designs tailored to the local acoustic environment. The resulting structure could then be fabricated using additive manufacturing and applied as a detachable acoustic interface between the tissue and the probe during ultrasound examinations. Although such a workflow remains to be validated experimentally and clinically, the present study demonstrates the feasibility of the underlying transmission-enhancement mechanism on which such patient-specific implementations could be built. Eventually, the proposed framework provides a pathway toward future adaptive or actively tunable acoustic metamaterials in patient-specific cases.

Imaging Artifacts and Flow. The ultrasound images (Fig. 4-(a)) demonstrate that the optimized MML increases acoustic energy transmission into the artery lumen and improves visualization of downstream vessel structures. Nevertheless, image artifacts generated by the microstructured metamaterial architecture still impede reliable EchoPIV analysis of the flowing microbubbles. In particular, the high-intensity inclined and cross-shaped patterns beneath the optimized MML, together with the apparent upward displacement of the vessel walls caused by the aberrating layer, remain visible. These artifacts are likely caused by a combination of scattering and phase aberration introduced by the metamaterial structure, whereas sound-speed mismatch is not expected to be the dominant factor due to the gradient impedance matching of the MML. Consequently, enhanced acoustic transmission does not automatically translate into proportional improvements in image quality or flow quantification. Future optimization efforts should therefore consider image-quality and flow-estimation metrics in addition to transmission performance. Practical considerations further include fabrication tolerances of the microstructured geometry, alignment between the acoustic beam and the structured interface, and the mechanical stability of the layer during probe contact, all of which may influence the intended impedance-matching effect. Previous work has demonstrated improved transmission behind moderately attenuating layers using iterative attenuation-correction schemes based on apodization and transmit-power modulation[23]. However, for highly reflective interfaces such as those considered here, increasing transmit power alone would also increase reflections and associated artifacts. Combining metamaterial-based transmission enhancement with advanced beamforming, aberration-correction, and image-processing approaches may therefore provide a promising route toward improved flow quantification in the presence of highly reflective vascular lesions.

Morphological Variability. An additional consideration for practical applications is the variability in plaque morphology and acoustic properties observed *in vivo*. Calcified plaques often exhibit heterogeneous composition, irregular surface roughness, and curved interfaces, which may influence the acoustic interaction with the proposed MML. In the present study, simplified geometries and material parameters were intentionally used to isolate and demonstrate the fundamental transmission-enhancement mechanism of the structured interface. In principle, however, the optimization framework can be extended to heterogeneous acoustic environments by adapting the structural parameters to the local anatomy and material properties. Furthermore, the current design is intended for relatively superficial vascular targets, where the MML can be positioned close to the aberrating structure. Extending the concept to deeper targets and more complex propagation paths remains an important topic for future investigation.

Broader Scope. Beyond calcified vascular plaques, the presented framework may be applicable to a broader range of ultrasound challenges involving highly reflective or aberrating structures, including bone-associated interfaces, implanted materials, and other heterogeneous tissues that limit acoustic penetration. More generally, the demonstrated ability to engineer acoustic transmission using additively manufactured microstructures establishes a foundation for customized metamaterial-assisted ultrasound imaging. While the present work focuses on passive structures, the proposed framework may also provide a pathway toward future adaptive or actively tunable acoustic metamaterials capable of combining transmission enhancement, aberration correction, and beam shaping within a single platform. Although such systems remain technologically challenging, the present study demonstrates that patient-specific acoustic interfaces can be systematically designed and fabricated for clinically relevant ultrasound frequencies, thereby opening new opportunities for metamaterial-assisted medical imaging.

Methods

This section describes the numerical, fabrication, and experimental procedures used to design, implement, and evaluate the proposed meta-matching layer (MML). The overall methodology follows a simulation-driven design framework, in which the structural parameters of the MML are optimized using numerical modeling and subsequently validated through experimental measurements. Numerical simulations were performed to analyze acoustic wave propagation and to guide the design of the triangular impedance-transition structures. The optimized designs were then fabricated using additive manufacturing techniques, and their acoustic performance was evaluated using controlled experimental setups, including pressure field measurements and ultrasound imaging in arterial phantoms. Additional details regarding the simulation framework, optimization procedure, and experimental configurations are provided to ensure consistency between the numerical and experimental investigations. The methods, alongside with the **Supplementary Materials**, are described in sufficient detail to enable reproducibility of the results and to allow independent validation by other researchers.

First MML Design

The first MML design is based on the concept of a graded acoustic impedance layer, achieved by gradually varying the solid fill fraction along the ultrasound propagation direction[11], as briefly explained in the Introduction section. Such graded structures are commonly used to reduce reflections at interfaces with strong impedance mismatch by providing a smooth effective transition between materials. In a simplified one-dimensional description, this transition can be represented by a spatially varying acoustic impedance profile $Z(x)$ across the layer thickness L, for example using a linear taper:

$$Z(x) = Z_1 + (Z_2 - Z_1)\frac{x}{L}, \tag{2}$$

where Z_1 and Z_2 are the acoustic impedances of the incident and transmission media, respectively, $x \in [0, L]$ is the spatial coordinate along the propagation direction, and L is the total thickness of the matching layer. This formulation illustrates how a gradual impedance transition can reduce reflections compared to an abrupt interface.

In this work, the gradient is implemented using a periodic array of triangular unit cells (a 2D version of 3D cones), with the apex of each triangle facing the incident ultrasound wave and the base facing the aberrating layer. This geometry produces a monotonic increase in the effective acoustic impedance through the layer.

The first meta-matching layer (MML, Fig. 2-(a)) was designed in COMSOL Multiphysics and its performance was assessed by frequency- and time-domain numerical simulations using material properties corresponding to the materials later used for fabrication. In these initial simulations it was assumed that the material of the MML and the plaque were loss free, and the main mechanism responsible for shadow artifacts was the impedance mismatch leading to energy loss due to reflection.

The geometric parameters of the unit cell were determined through an iterative parametric exploration guided by numerical transmission performance. As an initial guess, the value of h was fixed at 550 μm (a value smaller than the wavelength at 4 MHz), and w was varied at subwavelength values until a desirable transmission profile was achieved. Due to idealized conditions (no loss and no ASI), the Grid Search yielded near-unity transmission after only a few iterations, reaching transmission values close to 1 across the considered frequency band (1-4 MHz). This process resulted in unit cell dimensions of $h = 550\ \mu m$ and $w = 150\ \mu m$.

As mentioned, in this initial design stage, attenuation and acoustic–solid interactions were not considered. These assumptions led to high attenuation values in the first fabricated MML. Subsequent analysis that incorporated these effects, together with a systematic parameter sweep, led to different values of h and w (see Fig. 3). Note also that in the 2D design investigated in this paper, the unit cells are triangular with a base and height that fully characterize the geometry, assuming zero distance between neighboring unit cells.

MML Fabrication

The meta-matching layers (MMLs) were fabricated using a high-resolution micro-stereolithography (µSLA) 3D printer (MicroArch S240, Boston Micro Fabrication, USA), which enables additive manufacturing of complex microstructures with feature sizes down to 10 μm. This system utilizes a layer-by-layer projection printing technique based on digital light processing (DLP), wherein a digital micromirror device (DMD) selectively cures photopolymer resin at each layer by projecting spatially modulated ultraviolet light. The platform offers a build resolution of 10 µm or 5 µm depending on the resin and mode used, making it suitable for printing subwavelength structures tailored to MHz-range ultrasound[37].

Two main versions of the MML were fabricated for this study. The non-optimized MML was printed using Yellow 20 resin, a rigid photopolymer compatible with a 10 µm resolution setting. The optimized MMLs were printed using both Yellow 20 and Yellow 10 resins, with the latter enabling 5 µm resolution to capture finer details in the triangular ridges designed for improved acoustic performance. In both cases, the printer's exposure time, layer thickness, and shrinkage compensation parameters were fine-tuned to ensure dimensional fidelity of the high-aspect-ratio ridged structures. Under ideal conditions, the triangular structure was designed to have a height of 550 µm and a unit width of 150 µm. However, the initial printing parameters were set to a height of 860 µm, accounting for shrinkage, and a width of 150 µm. The initial fabricated superstructure was measured to have an actual height of only 400 µm, with a 150 µm discrepancy with respect to the intended value, attributed to improper settings of the printer's exposure energy and exposure time. To address this, we adjusted the printing parameters by reducing the exposure energy by 40 compared to the initial printing conditions and shortening the exposure time from 1.3 seconds to 0.8 seconds, improving the accuracy of the print. The printing precision for the conical superstructure was set at 10 µm per slice layer. For the distorted layers, the printing precision was set at 40 µm per layer across 25 layers. The optimal MML was printed with even better accuracy, with fabricated height and width close to the design values.

Following printing, the samples were rinsed in isopropyl alcohol to remove uncured resin. No post-curing under UV light was performed, as this would increase the stiffness of the material and consequently its acoustic impedance, potentially affecting wave transmission characteristics. The printed MMLs were examined under a bright-field microscope to verify structural integrity and dimensional accuracy. All MMLs were printed as monolithic parts and attached directly to the flat surface of the plaque model (SAL) to minimize air gaps and ensure good acoustic coupling in subsequent experiments.

Material Property Measurements

Attenuation and Speed of Sound Measurements

To characterize the acoustic properties of the 3D-printed samples, we used a through-transmission setup in a water tank, following the configuration described by in Ref.[38]. Two broadband ultrasound transducers (V307 SU as transmitter, V304 SU as receiver, both Olympus, USA) were positioned coaxially at a fixed distance, one acting as a transmitter and the other as a receiver (Fig. 5-(a)). Each sample was secured with a custom holder designed to ensure perpendicular alignment and minimize tilt. Two holders were available, as shown in Fig. 5-(a), but to prevent the holder from influencing the measurement of the samples, the black holder shown in the inset was used for all the MMLs (and repeat measurements of the SALs). This holder was glued to the top of each sample and were manually coded with a marker at their bottom. The experiment technical details are summarized in Table 1.

The speed of sound (SoS) in each sample was determined by comparing the time-of-flight (TOF) through the material with that in water. Let d denote the thickness of the sample, t_s the measured time-of-flight with the sample present, and t_w the TOF over the same distance in water. The SOS in the sample, c_s, was calculated as:

$$c_s = \frac{d}{t_s - t_w + \frac{d}{c_w}} \tag{3}$$

where c_w is the speed of sound in water, assumed to be 1480 m/s at room temperature[39].

Table 1. Two-transducer attenuation measurement setup

Category	Detail
Setup type	Through-transmission in water tank
Transducers	Olympus V307 SU (Tx), V304 SU (Rx)
Configuration	Coaxial alignment
Medium	Water at room temperature
Sample mounting	Custom holder containing a small window
Alignment	Perpendicular to propagation
Frequency range	1–5 MHz
Repetitions	50
Outputs	Speed of sound, attenuation
Water SoS	1480 m/s

Table 2. Acoustic properties of materials used in simulations. Impedance $Z = \rho \cdot c$ expressed in MPa·s/m (=MRayl).

Material	c (m/s)	ρ (kg/m^3)	Z (MRayl)	Reference
Water	1480	1000	1.478	Ref.[39]
Flexible 80A	1800	1130	2.034	Our measurement
Clear V4 (Formlabs)	2590	1178	3.051	Ref.[40]
Yellow-20 (BMF-HTL)	2550	1280	3.264	Our measurement

To determine attenuation, we used a frequency-domain approach by comparing the amplitude spectra of the received signals with and without the sample. Let $A_s(f)$ and $A_w(f)$ denote the spectral amplitudes at frequency f with and without the sample, respectively. The frequency-dependent attenuation coefficient $\alpha(f)$ was computed as:

$$\alpha(f) = 20\log_{10}\left(\frac{A_w(f)}{A_s(f)}\right) \tag{4}$$

Measurements were conducted across the 1–5 MHz frequency range, covering the operational bandwidth of the receiving transducer and the target frequency of 4 MHz. Each measurement was programmed to be repeated 50 times to ensure repeatability and reduce noise. This characterization enabled direct comparison of acoustic performance across MML and SAL samples, isolating the effect of trangular patterning on wave propagation.

After obtaining the performance results of the first MML, a methodic study was carried out to single out the reasons why the MML did not perform as expected. The factors included: (1) the lateral displacement with respect to the single-element transducer (focus effect), (2) the angle of the MML with respect to the ultrasound waves, measured relative to the axis parallel to the groves, (3) the angle of the MML with respect to the ultrasound waves, measured relative to the axis perpendicular to smooth, back-surface of the MML, (4) fabrication effect across multiple rounds of fabrication, (5) water penetration into the groves. The results of this study are presented in **Supplementary Materials A**, showing that the single most influential factor was the inherently high attenuation of the MML.

Table 2 summarizes the key acoustic properties (speed of sound, density, and acoustic impedance) of the materials used in our simulations. We initially used Clear V4 (Formlabs) for the plaque models (as in Fig. 1) but later switched to Yellow-20 (BMF-HTL resin), as it allowed fabrication of both the simple aberration layer (SAL) and the meta-matching layer (MML) together with sufficient resolution. As in the table, the acoustic impedance difference between Clear V4 and Yellow-20 is small, justifying the material change without significantly affecting impedance matching. As a side note, our initial effort at printing the MML using Clear V4 on Form 3 did not succeed due to insufficient resolution.

Compared to physiological values, we note that in the case of highly calcified plaques, the acoustic impedance may reach up to ≈2.5 MRayl[41,42]. Yellow-20 exhibits an impedance of ≈3.3 MRayl, exceeding the value reported for highly calcified plaques, approaching values for more severely calcified cases. This greater impedance implies that ultrasound compensation across such a material was more challenging than *in vivo*, effectively representing a worse aberration scenario.

Flexible 80-A has an impedance of ≈2.03 MRayl—closely matching the fibrous (collagen-rich) regions of arterial wall tissue, which have been measured via scanning acoustic microscopy in human carotid plaques to fall between 1.85 and 2.10 MRayl[43]. This supports the use of Flexible 80-A as a suitable surrogate for native arterial tissue in acoustic terms. We note that the referenced tissue measurements were obtained at high frequencies (e.g., 80 MHz in[43]), while our experimental measurements were conducted at 4 MHz. Although speed of sound may exhibit mild dispersion for tissue, the difference is

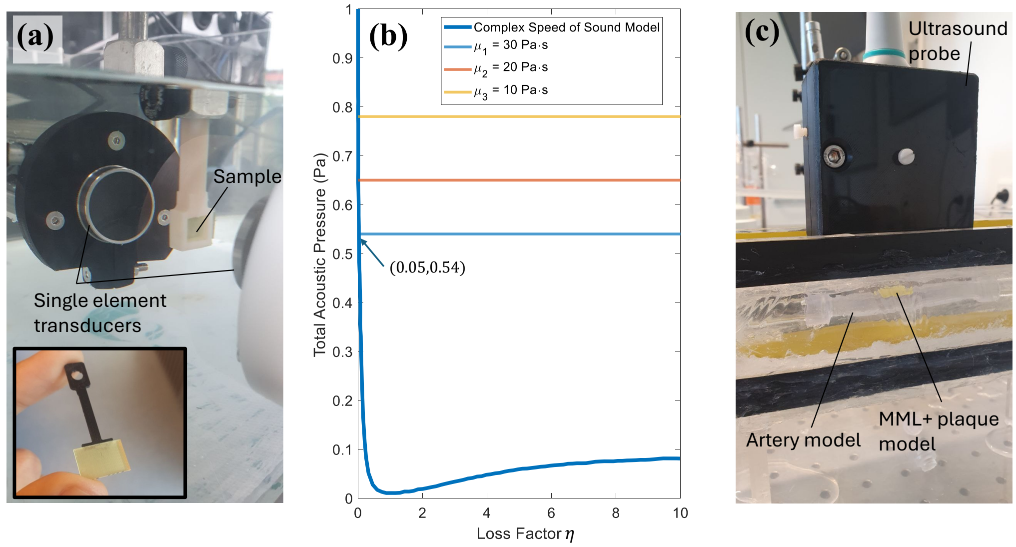

Figure 5. Material property measurements: (a) The attenuation and speed-of-sound measurement setup including two single element transducers, a sample holder, and water tank. (b) The loss factor retrieval method where a complex speed-of-sound model is used to find the loss factor that would lead to a transmission coefficient of 0.54 at 4 MHz. Thermo-viscous models enable defining a viscosity value associated with the amount of attenuation for time-domain simulations. (c) The ultrasound imaging setup including a probe holder, a water tank where the artery and plaque model are immersed and flow circuit (not shown) that circulates water and microbubbles through the artery model.

expected to be small. It is important to note that tissue density (ρ) is essentially frequency-independent, so dispersion primarily affects the speed of sound. Human tissue data—such as measurements on excised human myometrium and uterine fibroid tumors—show speed of sound varying by only about 4 to 14 m/s over the 1–3 MHz range[44]. Extrapolating conservatively to the 4 MHz vs. 80 MHz case ($\Delta f \approx 76$ MHz), one might predict a maximum SoS shift on the order of $\leq$ 50–60 m/s. Since $Z = \rho c$ and ρ stays constant, this corresponds to a change in impedance of $\leq$ 3–4 %. Therefore, despite the frequency difference between literature (80 MHz) and our measurements (4 MHz), the impedance comparisons remain robust between tissue and the photopolymers used.

Retrieval of the Loss Factor

To simulate the attenuation behavior of Yellow-20 in COMSOL Multiphysics, we used a frequency-domain approach where the material loss is introduced via the imaginary component of the speed of sound. The methodology included four key steps:

1. Calculating the Transmission Coefficient from Experimental Data Attenuation measurements (in dB) were converted into transmission coefficients using the standard relation:

$$\hat{\alpha} = -20 \cdot \log_{10}(|T|) \tag{5}$$

where $\hat{\alpha}$ is the attenuation in decibels and $|T|$ is the amplitude of the transmission coefficient. For example, an attenuation of 5.34 dB through 1 mm of Yellow-20 at 4 MHz corresponds to a transmission coefficient of $|T| = 0.54$.

2. Frequency-Domain Simulation Using a Complex Speed of Sound To replicate this transmission in simulation, we modeled the speed of sound c in Yellow-20 as:

$$c = c_0(1 + i \cdot \eta) \tag{6}$$

where c_0 is the measured speed of sound in Yellow-20 and η is a dimensionless loss factor. A sweep over the loss factor was performed, and the resulting absolute total acoustic pressure was recorded (Fig. 5-(b)). This approach enabled fitting the simulation response to the experimental transmission value.

3. Loss Factor Retrieval By identifying where the total acoustic pressure becomes equal to the measured $|T|$, as shown by a small arrow in Fig. 5-(b)), we retrieved a loss factor of 0.05, which accurately reproduces the experimental attenuation behavior. This loss factor was used in frequency-domain simulations to represent attenuation in Yellow-20.

4. Frequency-Domain Simulation with Thermal and Viscous Losses In a complementary simulation, we used COMSOL's thermo-viscous acoustics module to model attenuation through physical mechanisms. The dynamic viscosity of Yellow-20 was varied to match the transmission coefficient obtained experimentally. As shown in Fig. 5-(b), increasing the viscosity decreased the absolute total pressure. At a dynamic viscosity of 30 Pa·s, the simulated transmission coefficient matched the measured value of $|T| = 0.54$. This method can be used for time-domain simulations in COMSOL Multiphyiscs, where a complex speed of sound cannot be defined.

Estimation of Shear Speed of Sound in Solid Materials

To accurately simulate acoustic-solid coupling, both the longitudinal and shear speeds of sound in the solid medium must be known. While the longitudinal wave speed c_L can be measured directly via time-of-flight methods, the shear wave speed c_S can be calculated if the Young's modulus E, Poisson's ratio ν, and material density ρ are known. The relation between these quantities is given by the standard elasticity expression for longitudinal wave speed in an isotropic solid[45]:

$$c_L = \sqrt{\frac{E(1-\nu)}{\rho(1+\nu)(1-2\nu)}} \tag{7}$$

Rearranging this equation leads to a quadratic form in ν:

$$2\rho c_L^2 \nu^2 + (\rho c_L^2 - E)\nu + (E - \rho c_L^2) = 0 \tag{8}$$

Solving this quadratic yields two possible roots:

$$\nu_{1,2} = \frac{E - \rho c_L^2 \mp \sqrt{9\rho^2 c_L^4 - 10E\rho c_L^2 + E^2}}{4\rho c_L^2} \tag{9}$$

Using the positive root (as the Poisson's ratio must be between 0 and 0.5 for most solids), we obtain the value of ν, which can then be substituted into the shear wave speed formula:

$$c_S = \sqrt{\frac{E}{2\rho(1+\nu)}} \tag{10}$$

In our case, for the HTL Yellow 20 photopolymer, the Young's modulus was taken as $E = 2.4$ GPa according to the material datasheet[46], and the density $\rho = 1280$ kg/m^3 and longitudinal speed of sound $c_L = 2550$ m/s were measured experimentally. Substituting these values into Equation (2) and solving for ν gave $\nu = 0.45$. Plugging in this result in Equation (4), we calculated the shear wave speed to be $c_S = 798.6$ m/s. These parameters were then used in the Yellow-20 domains of our acoustic-solid interaction simulations in COMSOL Multiphysics.

Numerical Modeling

All simulations were performed using COMSOL Multiphysics 6.2, employing both the Pressure Acoustics, Frequency Domain module and the Acoustic-Solid Interaction multiphysics interface. The simulation domain consisted of a homogeneous background medium (water), with the meta-matching layer (MML) structure embedded between the acoustic source and the target interface (simple aberration layer (SAL), the same material as the MML). To account for physical losses, we incorporated acoustic attenuation into the model by defining the speed of sound as a complex quantity, where the imaginary component governs the frequency-dependent energy dissipation, as described in the previous subsection.

The computational domain was truncated using absorbing boundaries at the top and bottom boundaries and periodic conditions at the sides to eliminate spurious reflections. A plane-wave pressure field was launched toward the MML at a target frequency of 4 MHz, corresponding to the same frequency used in downstream experimental validation. Mesh refinement analysis was performed to ensure convergence. The output of interest was the transmission coefficient through the MML and the SAL underneath it, measured at the dashed line in Fig. 3-(a).

Optimization of the MML Features

The unit cell of the MML was defined as an isosceles triangular structure extruded in the out-of-plane direction (by a value exceeding 5 times the wavelength), approximating a locally invariant geometry along the propagation axis. Each unit cell was parameterized by its base width w and height h, normalized by the wavelength λ in the MML at 4 MHz, yielding $n_w = w/\lambda$ and $n_h = h/\lambda$.

Table 3. COMSOL simulation and optimization details

Category	Detail
Software	COMSOL Multiphysics 6.2
Modules	Pressure Acoustics (FD), Acoustic-Solid Interaction (ASI)
Excitation	Plane wave
Target Frequency	4 MHz
Boundary conditions	Absorbing (top/bottom), periodic (sides)
Loss modeling	$c = c_0(1 + i\eta)$
Loss factor	$\eta = 0.05$
Output	Transmission coefficient $\lvert T \rvert$
Optimization goal	**Maximize** $\lvert T \rvert$
Parameters	w, h
Normalization	$n_w = w/\lambda$, $n_h = h/\lambda$
Range	$n_w = 0.2$–3, $n_h = 0.2$–1
Step size for n_w and n_h	0.1
Optimization type	Parametric sweep (grid search)
Model levels	Lossless, loss, loss + ASI
Mesh	Fine, Convergence-tested

The optimization objective was to maximize the magnitude of the transmission coefficient $|T|$ at 4 MHz through the MML–plaque interface. For each parameter combination, the transmission and reflection coefficients were computed and compared to identify the configuration yielding the highest transmission.

A grid-based parametric sweep (Grid Search) was implemented using COMSOL Multiphysics coupled with MATLAB LiveLink, where n_w and n_h were systematically varied over the ranges $n_w = 0.2$–3 and $n_h = 0.2$–1, with step sizes of 0.1, resulting in 260 design configurations. The lower bound of 0.2 was imposed by fabrication constraints, specifically the resolution limits of the 3D printing process. The height parameter was restricted to subwavelength values ($n_h \leq 1$) to maintain a compact structured layer, while the width parameter was explored beyond the subwavelength regime to assess the impact of larger feature sizes (which turned out to lead to underperformance in transmission).

To assess the influence of physical effects on the optimal design, three progressively refined models were evaluated for each configuration: (1) a lossless pressure acoustics model, (2) a lossy acoustic model incorporating material attenuation, and (3) a fully coupled acoustic–solid interaction model including both fluid and solid domains. In the latter, the solid domain represents the 3D-printed Yellow 20 resin, with shear wave speeds obtained from the solid mechanics formulation described previously, enabling accurate modeling of mode conversion at fluid–solid interfaces.

The optimal MML geometry was selected based on the maximum transmission coefficient across all evaluated configurations. The numerical model, optimization workflow, and implementation details are provided in Supplementary Materials D and E. The key simulation parameters and optimization settings are summarized in Table 3.

Ultrasound Imaging and Flow Phantom Setup

Ultrasound imaging was performed using a Verasonics Vantage 128 system (Verasonics Inc., Kirkland, USA) equipped with an L12-3v linear array transducer (nominal center frequency of 7.5 MHz). Plane-wave imaging at various frequencies and speed of 2000 frames/s was used to acquire high-frame-rate ultrasound data. The selected transmit frequencies (3–6 MHz) lie within its broadband response, and the effective bandwidth is determined by the probe characteristics. Image reconstruction was performed assuming a constant speed of sound of 1540 m/s, consistent with standard clinical ultrasound settings. No sound-speed correction was applied to maintain clinically relevant imaging conditions.

In contrast to our previous setup[47], where a Vivitro flow pump was used, flow was driven here using a Masterflex peristaltic pump, alongside with a pulsation dampener (Cole-Parmer, USA), offering compact control and minimizing pulsatility during image acquisition. A total of 50 frames were acquired per measurement and were averaged to produce a single high-quality image for intensity-based analysis, reducing the influence of temporal fluctuations and noise.

As shown in Fig. 5-(c), the flow phantom consisted of a tissue-mimicking vessel, made of Flexible-80A (Formlabs, USA) embedded in a water tank, oriented for lateral scanning. To facilitate the precise placement of the meta matching layer (MML), the vessel cross section was changed to be square rather than the conventional circular shape. This geometry ensured direct contact between the MML and the phantom surface while preserving acoustic accessibility. In-house microbubbles (by Physics of Fluid Group, University of Twente) were circulated through the phantom to create backscatter for image intensity analysis, and all experiments were conducted at room temperature under constant flow conditions. The ultrasound imaging and flow

Table 4. Ultrasound imaging experiment setup

Category	Detail
System	Verasonics Vantage 128
Transducer	L12-3v linear array
Imaging mode	Plane-wave imaging
Frame rate	2000 frames/s
Frequencies	3–6 MHz
Number of frames	50
Medium	Water at room temperature
Phantom	Flexible 80A vessel model
Flow system	Masterflex peristaltic pump
Flow control	Pulsation dampener
Contrast agent	In-house microbubbles from PoF

experiment details are summarized in Table 4.

Conclusion

In this proof-of-concept study, we introduced and experimentally validated one of the first additively manufactured meta-matching layer (MML) designed for MHz-range ultrasound, specifically targeting transmission improvement through calcified vascular plaques. Through a two-stage design process—starting with idealized lossless models and progressing to more realistic simulations including acoustic-solid interactions and material attenuation—we demonstrated that high-resolution 3D printing can realize subwavelength gradient-impedance structures that meaningfully affect wave propagation at 4 MHz. Experimental results confirmed enhanced forward transmission and reduced reflection compared to simple aberration layers, although some limitations such as increased structural artifacts and the inability to fully restore shadowed regions remain. Nonetheless, this work establishes the viability of customizable, passive metamaterial add-ons for clinical ultrasound systems, potentially enabling patient-specific imaging enhancement in plaque-heavy regions, as well as in other medical imaging applications. Future directions include exploring a broader range of printable materials, integrating artifact-suppression algorithms, and extending the design framework to account for lateral and depth-dependent tissue heterogeneity. These findings lay the groundwork for a new class of 3D-printed acoustic metamaterials in medical imaging applications.

Funding

This work was funded by the Netherlands Organisation for Health Research and Development (ZonMw) under the OffRoad grant scheme (Grant No. 04510012210058).

References

1. Park, C. M. & Lee, S. H. Zero-reflection acoustic metamaterial with a negative refractive index. *Sci. reports* **9**, 3372 (2019).
2. Zhang, S., Yin, L. & Fang, N. Focusing ultrasound with acoustic metamaterial network. *Phys. Rev. Lett.* (2009).
3. Luyun, C. & Xichun, H. Acoustic cloaking design based on penetration manipulation with combination acoustic metamaterials. *J. Low Freq. Noise, Vib. Active Control.* **43**, 429–436 (2024).
4. Ghanbarzadeh-Dagheyan, A., Molaei, A., Heredia-Juesas, J. & Martinez-Lorenzo, J. A. Application of a resonant metamaterial line array in ultrasound compressive imaging. In *ASME International Mechanical Engineering Congress and Exposition*, vol. 52163, V011T01A026 (American Society of Mechanical Engineers, 2018).
5. Cummer, S. A., Christensen, J. & Alù, A. Controlling sound with acoustic metamaterials. *Nat. Rev. Mater.* **1**, 1–13 (2016).
6. Ge, H. *et al.* Breaking the barriers: advances in acoustic functional materials. *Natl. Sci. Rev.* **5**, 159–182 (2018).
7. Dong, E. *et al.* Underwater acoustic metamaterials. *Natl. Sci. Rev.* **10**, nwac246 (2023).
8. Qin, F., Zhang, J. & Drinkwater, B. W. The effects of manufacturing errors on the performance of acoustic metamaterial lenses operating in the mhz regime. *Small Sci.* **5**, 2400481 (2025).

9. Wang, J., Allein, F., Boechler, N., Friend, J. & Vazquez-Mena, O. Design and fabrication of negative-refractive-index metamaterial unit cells for near-megahertz enhanced acoustic transmission in biomedical ultrasound applications. *Phys. Rev. Appl.* **15**, 024025 (2021).

10. Pedersen, P. C., Tretiak, O. & He, P. Impedance-matching properties of an inhomogeneous matching layer with continuously changing acoustic impedance. *The J. Acoust. Soc. Am.* **72**, 327–336 (1982).

11. Li, Z. *et al.* Broadband gradient impedance matching using an acoustic metamaterial for ultrasonic transducers. *Sci. reports* **7**, 42863 (2017).

12. Albay, M. M. *et al.* Metamaterial-integrated bioadhesive hydrogel transducer for long-term ultrasound monitoring. *Adv. Mater. Technol.* e01623 (2026).

13. Ji, H.-w. *et al.* Design of acoustic impedance gradient matching layers. *Appl. Acoust.* **211**, 109549 (2023).

14. Lan, J., Li, Y., Xu, Y. & Liu, X. Manipulation of acoustic wavefront by gradient metasurface based on helmholtz resonators. *Sci. reports* **7**, 10587 (2017).

15. Andrés, D., Carrión, A., Camarena, F. & Jiménez, N. Methods to design and evaluate transcranial ultrasonic lenses using acoustic holography. *Phys. Rev. Appl.* **20**, 044071 (2023).

16. Melde, K., Mark, A. G., Qiu, T. & Fischer, P. Holograms for acoustics. *Nature* **537**, 518–522 (2016).

17. Jiménez-Gambín, S. *et al.* Acoustic holograms for bilateral blood-brain barrier opening in a mouse model. *IEEE Transactions on Biomed. Eng.* **69**, 1359–1368 (2021).

18. Li, L., Diao, Y., Wu, H. & Jiang, W. Complementary acoustic metamaterial for penetrating aberration layers. *ACS Appl. Mater. & Interfaces* **14**, 28604–28614 (2022).

19. Chen, T. *et al.* Enhanced ultrasound transmission through skull using flexible matching layer with gradual acoustic impedance. *ACS Appl. Mater. & Interfaces* **15**, 55510–55517 (2023).

20. Mohebali, J. *et al.* Acoustic shadowing impairs accurate characterization of stenosis in carotid ultrasound examinations. *J. vascular surgery* **62**, 1236–1244 (2015).

21. van Helvert, M. *et al.* High-frame-rate contrast-enhanced ultrasound particle image velocimetry in patients with a stented superficial femoral artery: a feasibility study. *Eur. radiology experimental* **6**, 32 (2022).

22. Engelhard, S. *et al.* Blood flow quantification with high-frame-rate, contrast-enhanced ultrasound velocimetry in stented aortoiliac arteries: in vivo feasibility. *Ultrasound Medicine & Biol.* **48**, 1518–1527 (2022).

23. Plomp, J., Ghanbarzadeh-Dagheyan, A., Versluis, M., Lajoinie, G. & Jebbink, E. G. Imaging behind the plaque: Improved blood flow quantification using an iterative scheme for active attenuation correction. *Ultrasound Medicine & Biol.* **51**, 984–998 (2025).

24. Kips, J. G., Segers, P. & Van Bortel, L. M. Identifying the vulnerable plaque: A review of invasive and non-invasive imaging modalities. *Artery Res.* **2**, 21–34 (2008).

25. Klopfenstein, R. W. A transmission line taper of improved design. *Proc. IRE* **44**, 31–35 (1956).

26. Pozar, D. M. *Microwave Engineering* (Wiley, 2011), 4th edn.

27. Ji, H.-w. *et al.* Design of acoustic impedance gradient matching layers. *Appl. Acoust.* **211**, 109549 (2023).

28. Chen, T. *et al.* Enhanced ultrasound transmission through skull using flexible matching layer with gradual acoustic impedance. *ACS Appl. Mater. & Interfaces* **15**, 55510–55517 (2023).

29. Lewińska, M. A., Kouznetsova, V. G., van Dommelen, J. A. W., Krushynska, A. O. & Geers, M. G. D. The attenuation performance of locally resonant acoustic metamaterials based on generalised viscoelastic modelling. *Int. J. Solids Struct.* **126**, 163–174, DOI: 10.1016/j.ijsolstr.2017.08.003 (2017).

30. Craig, S. R., Welch, P. J. & Shi, C. Non-hermitian complementary acoustic metamaterials for imaging through skull with imperfections. *Front. Mech. Eng.* **6**, Article 55, DOI: 10.3389/fmech.2020.00055 (2020).

31. Oglat, A. A. *et al.* A review of medical doppler ultrasonography of blood flow in general and especially in common carotid artery. *J. medical ultrasound* **26**, 3–13 (2018).

32. Choi, H.-Y. Carotid duplex ultrasound: interpretations and clinical applications. *Annals Clin. Neurophysiol.* **23**, 82–91 (2021).

33. Bianchini, E. *et al.* The ultrasound window into vascular ageing: a technology review by the vascagenet cost action. *J. Ultrasound Medicine* **42**, 2183–2213 (2023).

34. Shi, H., Varghese, T., Dempsey, R. J., Salamat, M. S. & Zagzebski, J. A. Relationship between ultrasonic attenuation, size and axial strain parameters for ex vivo atherosclerotic carotid plaque. *Ultrasound Medicine & Biol.* **34**, 1666–1677, DOI: 10.1016/j.ultrasmedbio.2008.02.014 (2008).

35. Shi, H. *et al.* In vivo attenuation and equivalent scatterer size parameters for atherosclerotic carotid plaque: Preliminary results. *Ultrasonics* **49**, 779–785, DOI: 10.1016/j.ultras.2009.06.004 (2009).

36. Machado, J. C., Foster, F. S. & Gotlieb, A. I. Measurement of the ultrasonic properties of human coronary arteries in vitro with a 50-mhz acoustic microscope. *Braz. J. Med. Biol. Res.* **35**, 895–903, DOI: 10.1590/s0100-879x2002000800006 (2002).

37. Boston Micro Fabrication (BMF). Bmf reveals the microarch s240. https://bmf3d.com/news/bmf-reveals-the-microarch-s240 (2023). Accessed: 2025-08-05.

38. Mirgolbabaee, H. *et al.* Vascular flow phantom of a cohort-based averaged abdominal aortic aneurysm: Design, fabrication and characterization. *Annals Biomed. Eng.* **53**, 1439–1452, DOI: 10.1007/s10439-025-03717-y (2025). Epub 1 Apr 2025.

39. Marczak, W. Water as a standard in the measurements of speed of sound in liquids. *The J. Acoust. Soc. Am.* **102**, 2776–2779, DOI: 10.1121/1.420332 (1997).

40. Bakaric, M., Miloro, P., Javaherian, A. & Brown, M. D. Measurement of the ultrasound attenuation and dispersion in 3d-printed photopolymer materials from 1 to 3.5 mhz. *The J. Acoust. Soc. Am.* **150**, 2798–2805, DOI: 10.1121/10.0006668 (2021).

41. Bilen, B. T. Designating vulnerability of atherosclerotic plaques. In *Lipid Peroxidation Research*, 101–116 (IntechOpen, 2019).

42. Bilen, B. *et al.* Scanning acoustic microscopy and time-resolved fluorescence spectroscopy for characterization of atherosclerotic plaques. *Sci. Reports* **8**, 14378 (2018).

43. Tanaka, M. *et al.* Scanning acoustic microscopy and time-resolved fluorescence spectroscopy for characterization of atherosclerotic plaques. *Sci. Reports* **8**, 13082, DOI: 10.1038/s41598-018-32788-2 (2018).

44. Authors. Attenuation coefficient and sound speed in human myometrium and uterine fibroid tumors. *Ultrasound Medicine & Biol.* **27**, 1065–1071 (2001). Reports sound speed variation of approximately 4–14 m/s over 1–3 MHz in human tissues.

45. Brown University. Wave propagation in solids: Longitudinal and shear wave speeds. https://www.brown.edu/Departments/Engineering/Courses/En1750/Notes/Dynamics/Dynamics.htm (n.d.). Accessed: 2025-07-30.

46. Boston Micro Fabrication. HTL Yellow 20 Material Data Sheet. https://bmf3d.com/wp-content/uploads/2024/02/24-BMF-0029-Data-Sheet-Updates-HTL-Resin-PRINT-V2.pdf (2024). Accessed: 2025-07-30.

47. Ghanbarzadeh-Dagheyan, A. *et al.* Swirling flow quantification in helical stents using ultrasound velocimetry. *J. Endovascular Ther.* DOI: 10.1177/15266028241283326 (2024).

Acknowledgements

The authors would like to thank Prof. Erik Groot Jebbink for helping in ideation and grant acquisition, Prof. Guillaume Lajoinie for kindly sharing the ultrasound attenuation measurement setup and associated analysis code, and Prof. Michel Versluis and the Physics of Fluids group at University of Twente for providing the in-house microbubbles.

Author contributions statement

Conceptualization: A.G.D., E.D., C.S.; **Methodology:** A.G.D., E.D., C.S., M.G.; **Software:** A.G.D., E.D.; **Validation:** A.G.D., E.D.; **Formal analysis:** A.G.D.; **Investigation:** A.G.D., E.D., M.G.; **Resources:** A.G.D., C.S., N.F.; **Data curation:** A.G.D.; **Writing – Original Draft:** A.G.D., E.D., M.G.; **Writing – Review & Editing:** A.G.D., E.D., C.S., M.G.; **Visualization:** A.G.D.; **Supervision:** A.G.D., C.S., N.F.; **Project administration:** A.G.D.; **Funding acquisition:** A.G.D.

Data availability

The datasets used and/or analysed during the current study available from the corresponding author on reasonable request.

Competing Interests

The authors declare no competing interests.